ORIGINAL PAPER

Impact of 2D engine nacelle flow on buffet

Thomas Lürkens[1] · Matthias Meinke[1,2] · Wolfgang Schröder[1,2]

Abstract

Numerical studies on the interaction of nacelle and airfoil shock dynamics are performed. To keep the computational cost at an acceptable level, first 2D investigations on the interaction of nacelle and airfoil are performed that cover basic dynamic phenomena of this configuration. The transonic flow around the OAT15A airfoil is computed at buffet conditions, i.e., freestream Mach number $Ma_\infty = 0.73$, chord-based freestream Reynolds number $Re_c = 2 \cdot 10^6$, and angle of attack $\alpha = 3.5°$ using wall-modeled LES. Two configurations are considered, one which includes a generic 2D ultra-high bypass ratio (UHBR) engine nacelle geometry and one without an engine, which is denoted the baseline case. In addition to the airfoil shock, the flow field of the nacelle configuration is characterized by a shock wave on the upper part of the nacelle. Furthermore, the introduction of the UHBR-engine nacelle leads to a reduced effective angle of attack and Mach number in the flow to the airfoil. The changes in the topology of the flow to the airfoil caused by the nacelle lead to a reduced strength of the airfoil shock and a less developed buffet, which resembles the behavior close to the stability limit. The reduced shock dynamics yields lower pressure fluctuations at the airfoil trailing edge. A frequency analysis of time series data from the airfoil shock location shows a reduction of the buffet frequency for the nacelle configuration. Further investigations of the flow field dynamics using sparsity-promoting dynamic mode decomposition reveal a mutual mode between the airfoil shock and the nacelle shock. The existence of this mode has consequences for future investigations of nacelle airfoil interaction in transonic flow.

Keywords Transonic buffet · Engine nacelle flow · Wall-modeled LES

List of symbols

Greek symbols

α	Angle of attack
β	Penalty factor
γ	Heat capacity ratio
κ	Von Karman's constant
λ_i	Complex frequency
μ	Dynamic viscosity
μ_i	Ritz eigenvalue
ν	Kinematic viscosity
$\boldsymbol{\omega}$	Vorticity vector
ϕ_n	Spatio-temporal mode
ρ	Density
σ	Standard deviation
τ	Shear stress

Latin symbols

a_i	Amplitude of dynamic mode
c	Chord length
c_f	Skin friction coefficient
c_p	Pressure coefficient
h_{wm}	Wall-model sampling distance
$\boldsymbol{L}$	Lamb vector
L	Length
Ma	Mach number
Re	Reynolds number
Sr	Strouhal number
$\boldsymbol{u}$	Velocity vector

✉ Thomas Lürkens
   t.luerkens@aia.rwth-aachen.de

   Matthias Meinke
   m.meinke@aia.rwth-aachen.de

   Wolfgang Schröder
   office@aia.rwth-aachen.de

1 Chair of Fluid Mechanics and Institute of Aerodynamics, RWTH Aachen University, Wüllnerstraße 5a, Aachen 52062, Germany

2 JARA Center for Simulation and Data Science, RWTH Aachen University, Seffenter Weg 23, Aachen 52074, Germany

Indices

$'$	Perturbed quantity
∞	Freestream
nac	Related to the nacelle
oat	Related to the airfoil
$\parallel$	Wall-parallel
$+$	Inner units
w	At the wall
wm	Wall-model

Abbreviations

CFL	Courant–Friedrichs–Lewy
CTU	Convective time unit
DMD	Dynamic mode decomposition
SP-DMD	Sparsity-promoting dynamic mode decomposition
FFT	Fast Fourier transform
LES	Large-eddy simulation
MILES	Monotone integrated large-eddy simulation
UHBR	Ultra-high bypass ratio
WM-LES	Wall-modeled large-eddy simulation

1 Introduction

In transonic flow on wings of transport aircraft, a local supersonic region is formed that is terminated by a shock wave. The buffet phenomenon is characterized by a self-sustained large-scale oscillation of this shock wave at low frequencies in the range of $Sr \sim \mathcal{O}(10^{-2}) - \mathcal{O}(10^{-1})$ where $Sr = \frac{fc}{u_\infty}$ is the non-dimensional frequency denoted as Strouhal number. The spatial oscillation of the shock wave leads to periodically alternating forces on the wing structure. The structural response to those dynamic loads, generally referred to as buffeting, have detrimental effects on the structural integrity and overall flight safety. Therefore, it defines a strict boundary to an aircraft's flight envelope. Economical and ecological challenges require aviation to make ever more efficient use of the available resources. A thorough knowledge of the aeroelastic behavior of aircraft is crucial in the endeavor to further reduce structural weight and optimize fuel consumption. Therefore, a comprehensive understanding of the buffet phenomenon is substantially important in the design process of future aircraft.

Although the buffet phenomenon has been intensively investigated for decades a comprehensive description of the underlying mechanisms is still subject to debate. The most widely accepted model explaining the self-sustained nature of the low-frequency shock oscillation has been introduced by Lee [1]. The proposed mechanism is based on a closed feedback loop between the shock wave and the trailing edge flow. The interaction of the incoming boundary layer with the shock wave leads to the generation of vortices which convect downstream and eventually pass over the trailing edge. The transition from a wall-bounded flow to a free-shear layer causes the generation of pressure waves which propagate back upstream. The pressure waves interact with the shock wave and push the shock upstream leading to a thickening and ultimately a separation of the boundary layer downstream of the shock. The separation of the boundary layer mitigates or massively reduces the local wall-shear stress near the trailing edge flow. Thus, also the generation of pressure waves at the trailing edge is attenuated due to the decreased Lamb vector, i.e., the outer product of vorticity and the velocity vectors, and the shock moves back downstream closing the feedback loop. Good agreement with the buffet model proposed by Lee was found, among others, by Deck [2], Xiao et al. [3], Hartmann et al. [4–6] and Feldhusen-Hoffmann et al. [7, 8]. Lee's model was further developed by Hartmann et al. [6], who proposed that the relevant interaction region of the shock wave and the pressure waves originating from the trailing edge is at the upper part of the shock wave instead of the shock foot. This formulation led to a significantly better agreement between the predicted and the measured buffet frequency.

In the pursuit to design ever more efficient aircraft, engine development is clearly moving toward larger and larger bypass ratios, so-called ultra-high bypass ratio (UHBR) turbofan engines. The large diameter of such engines requires them to be mounted closely under the wing to ensure sufficient ground clearance without having to massively redesign the landing gear much more generously. As a result, the flow around the wing is significantly affected by the engine flow. In transonic flight, shock waves with all their detrimental effects, i.e., shock-induced separation, shock unsteadiness, and total pressure loss, can occur on the engine nacelle [9–11]. The buffet phenomenon is, however, highly sensitive to the upstream flow conditions, which are strongly altered by an upstream shock wave. Furthermore, the shear layer developing on the engine nacelle merges into the boundary layer on the pressure side of the airfoil. As a result, also the flow in the vicinity of the trailing edge is influenced by the integration of UHBR engines. Since the trailing edge flow is a central element to trigger shock wave oscillations [1, 6], the quality of the buffet phenomenon can be significantly affected.

In recent years, the buffet phenomenon has been studied extensively [1–8, 12, 13]. Yet, little is known about the interaction of engine induced flow disturbances and the involved dynamics. A recent experimental study by Spinner and Rudnik [11] investigates the phenomenon of shock buffet on the lower surface of the wing, which occurs at negative angles of attack due to the integration of the UHBR. To the best of the authors' knowledge, studies on the impact of engine nacelle integration on the buffet phenomenon on the upper wing surface do not exist in the archival literature. Yet, engine nacelle

integration is an important aspect of the aerodynamic design of commercial aircraft. This means it is of great interest to complement the current knowledge by the effect of engine-induced flow disturbances on the buffet phenomenon.

In this paper, first 2D studies are made to better understand the interaction between engine-induced upstream disturbances of the flow field and the buffet phenomenon on the suction side of the airfoil. Using wall-modeled large-eddy simulations (WM-LES) the flow field around the OAT15A airfoil with a generic UHBR-engine nacelle geometry and a baseline configuration without the nacelle is computed at buffet conditions. To allow the analysis of the upstream shock and the free-shear layer interacting with the airfoil boundary layer at reasonable computational cost the nacelle is modeled as a 2D-periodic flow-through nacelle. The flow-through nacelle essentially reduces the engine nacelle to a hollow body. The pylon has not been considered due to the inherently three-dimensional nature of the vortex pair emerging from the junction of the pylon to the nacelle. This means that the interaction of the nacelle and the airfoil shock is investigated without any flow phenomena generated by the pylon. Therefore, the current study is to be understood as a preliminary investigation focusing on the impact a geometric perturbation located upstream of the airfoil has on the flow structure of the airfoil and the resulting shock dynamics. Sparsity-promoting dynamic mode decomposition (SP-DMD) is used to extract dynamic features from the flow field and associate them with physical phenomena.

The paper is organized as follows. In Sect. 2, the simulation framework and the numerical methods are briefly presented. In particular, the wall-modeling approach is discussed in Sect. 2.1 and the SP-DMD algorithm is introduced in Sect. 2.2. The computational setup including the numerical mesh and the mesh refinement strategy is discussed in Sect. 3. The results are presented in Sect. 4 with Sect. 4.1 focusing on direct insights from the WM-LES. The results obtained performing SP-DMD on the simulation data are discussed in Sect. 4.2. Finally, conclusions are drawn in Sect. 5.

2 Numerical methods

All simulations are performed using the Cartesian solver of the m-AIA framework which was formerly denoted zonal flow solver (ZFS) [14]. The governing equations are the compressible, unsteady Navier–Stokes equations. The equations are spatially filtered and solved on an unstructured, hierarchical Cartesian mesh using the finite-volume method. The advective upstream splitting method (AUSM) is used for the convective fluxes. A central difference scheme is employed for the discretization of the viscous fluxes. For the temporal integration, a second-order accurate 5-stage

Runge–Kutta method is used. Small-scale turbulence is accounted for by the approach of monotone integrated LES (MILES) [15] such that no additional turbulence model is necessary [16]. Boundaries of embedded bodies are realized using a cut-cell method [17]. Further details on the numerical methods used by the m-AIA simulation framework are given in Meinke et al. and Schneiders et al. [16, 17].

2.1 Wall-stress model

Traditional wall-resolved LES of boundary layer flows are restricted by the resolution of the viscous sublayer which requires extremely small cells at high Reynolds numbers. This results in a large amount of mesh cells and thus in a enormous demands on the available computer hardware that often cannot be fulfilled. At the same time, the computational time step is restricted by the CFL condition and viscous stability leading to a very slow progress of the simulation in terms of convective time units $CTU = c/u_\infty$ making wall-resolved LES of high Reynolds number flows computationally very expensive. Wall-modeling approaches are a convenient method to circumvent the massive constraints on mesh resolution for traditional LES of boundary layer flows while maintaining a high spatial and temporal resolution. Omitting the resolution of the viscous sublayer and only resolving large-scale structures in the boundary layer WM-LES enables not only a significant reduction in the total number of cells but does also allow a substantially larger computational time step. Thereby, LES of dynamic phenomena at low Strouhal numbers $Sr = \frac{f \cdot c}{u_\infty}$ such as the buffet phenomenon can be performed even at high Reynolds numbers with reasonable computational effort. The applicability of such a wall-stress model to buffet flows has been demonstrated by Fukushima and Kawai [19].

In this study, an analytical wall-stress model is used to compute the wall-shear stress based on flow information obtained from the outer boundary layer. The function is an implicit single equation expression for the law of the wall introduced by Spalding [20]:

$$y^+ = u^+ + e^{-\kappa B}\left\{ e^{\kappa u^+} - \sum_{n=0}^{4} \frac{(\kappa u^+)^n}{n!} \right\} \quad (1)$$

with $u^+ = \frac{u_\parallel}{u_\tau}$, $y^+ = \frac{h_{wm} u_\tau}{\nu}$, and $u_\tau = \sqrt{\tau_w/\rho_w}$. The subscript $(\bullet)_\parallel$ denotes projection onto the wall-tangential plane. The von Kármán constant κ is set to 0.4 and B is 5.0. Equation 1 is evaluated at a sampling distance $y = h_{wm}$ normal to the surface which is illustrated in Fig. 1. The implicit expression is solved iteratively for u_τ using Newton's method. To apply the wall-shear stress to the boundary surface an additional correction loop within the viscous flux computation is
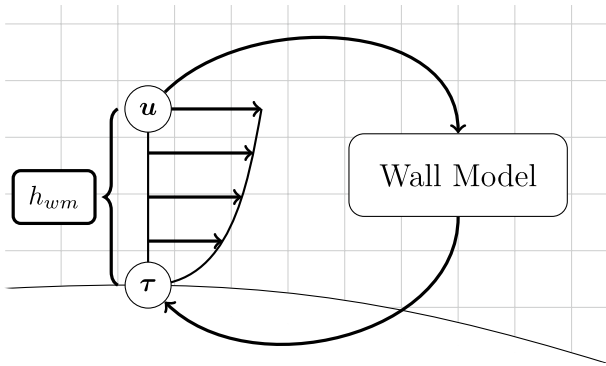
Fig. 1 Graphic representation of the wall-model mechanism, by courtesy of Lürkens et al. [18]

performed adding an artificial viscosity μ_{wm} such that the wall-shear stress given by

$$\left(\mu + \mu_{wm}\right)\frac{\partial u_\parallel}{\partial n} = \tau_{wm} \tag{2}$$

is imposed. To prevent an obvious misapplication of the model in regions of separated flow the velocity gradient at the wall is checked for $\partial u_\parallel / \partial n < 0$. If flow separation is detected, the application of the wall-stress model is omitted by setting $\mu_{wm} = 0$.

2.2 Dynamic mode decomposition

The dynamic mode decomposition [21] is a data-driven technique that allows the decomposition of a given data field $q(x, t)$ into a series representation of spatio-temporal modes ϕ_n. Every mode is characterized by an individual, complex frequency λ_n, and amplitude a_n. The resulting series representation of the data field reads

$$q(x, t) = \sum_n a_n e^{\lambda_n t} \phi_n(x). \tag{3}$$

For these modes, characteristic dynamic phenomena of distinct frequencies can be determined and analyzed in detail. The buffet phenomenon is typically restricted to narrow frequency bands such that DMD can be an effective tool for the in-depth analysis of the isolated dynamics and the underlying physical mechanisms, which is reflected by its frequent use in the literature [8, 22–25]. In general, a DMD performed on a set of N snapshots results in $N-1$ modes, which are given as complex conjugate pairs. For a large number of snapshots this results in an inconveniently large number of modes to assess. The sparsity-promoting DMD algorithm proposed by Jovanović et al. [26] addresses this problem by introducing a penalty term $\beta \sum_{n=1}^{N-1} |a_n|$ into the minimization problem determining the modes, which reads

$$\underset{a}{\text{minimize}} \ \|V_1^{N-1} - \Phi D_a V_{and}\|_F^2 + \beta \sum_{n=1}^{N-1} |a_n| . \tag{4}$$

Here, V_1^{N-1} is the discrete snapshot sequence and Φ contains the dynamic modes given in matrix form by

$$V_1^{N-1} = [v_1, v_2, \ldots, v_{N-1}], \quad \Phi = [\phi_1, \phi_2, \ldots, \phi_{N-1}]. \tag{5}$$

The matrix $D_a = \text{diag}(a)$ is the diagonal matrix of all optimized amplitudes a_n. The Vandermonde matrix V_{and} contains the so-called Ritz eigenvalues $\mu_n = e^{\lambda_n \Delta t}$ and reads

$$V_{and} = \begin{pmatrix} 1 & \mu_1 & \cdots & \mu_1^{N-1} \\ 1 & \mu_2 & & \mu_2^{N_1} \\ \vdots & \vdots & & \vdots \\ 1 & \mu_{N-1} & & \mu_{N-1}^{N-1} \end{pmatrix}. \tag{6}$$

When solving the minimization problem given by expression 4, increasing values of the penalty parameter β imply a stronger penalization of non-zero amplitudes, and thus result in an overall lower number of non-zero amplitude modes. More details on the SP-DMD algorithm are given in Jovanović et al. [26]. The application of SP-DMD to transonic buffet is thoroughly discussed in Feldhusen-Hoffmann et al. [8].

3 Computational setup

In the following, the computational setup of the nacelle configuration is presented. The baseline and the nacelle configuration both feature the OAT15A airfoil, the geometry of which was provided by courtesy of and upon request from ONERA. Note that except for the integration of the nacelle geometry the baseline configuration, i.e., no engine is taken into account, and the UHBR-airfoil configuration, and the corresponding mesh refinement both setups are identical and, therefore, no further differentiation is made unless otherwise necessary. A setup with only mild flow separation while still providing low-frequency shock oscillations is considered. Based on the work by Fukushima and Kawai [19], Jacquin et al. [13] and Deck [2], the angle of attack was set to $\alpha = 3.5°$ and the freestream Mach number to $Ma_\infty = 0.73$. In agreement with the associated experimental campaign by Schauerte and Schreyer [27], the chord-based Reynolds number was set to $Re_c = 2 \cdot 10^6$.

For the nacelle, a generic configuration based on a NACA 0012 airfoil was generated. The outer geometry of the nacelle geometry with respect to the local chord length is roughly based on the UHBR flow-through nacelle by Spinner and Rudnik [10], which was designed for the Airbus XRF-1 research model. That is, the inlet and the outlet diameter were set to $d_{nac} = 0.45c$ and the nacelle

length to $l_{nac} = 0.75c$. The nacelle trailing edge is located at $(x, y) = (0c, -0.075c)$ with respect to the airfoil leading edge.

The grid dimensions in the x-, y-, and z-coordinate directions $L_x \times L_y \times L_z = 25.4c \times 24.9c \times 0.05c$, which proved to be sufficient for comparable flows by Zauner and Sandham [28] and Moise et al. [29]. Figure 3 shows the mean pressure in the farfield at a distance of $R = 11c$ around the center of the airfoil at $(x, y) = (0.5c, 0.0c)$. The deviations from p_∞ are minimal. Note that the spanwise extent of the domain is still possibly too small to accommodate for the full development of large 3D structures. Since both cases—with and without nacelle—are subject to almost identical farfield conditions, the results are expected to be comparable as far as the qualitative variations of the distributions are concerned.

The grid is locally refined within the boundary layer satisfying the mesh requirements for WM-LES proposed by Kawai and Larsson [30], i.e., at least 20 cells are located within the boundary layer at $x_{oat} = 0.2c$ and $x_{nac} = 0.2c$. Since the acoustics in the vicinity of the trailing edge is a key element of established buffet models, additional a-priori refinement is applied on the suction side of the airfoil and in the wake region of the airfoil and the nacelle. The Cartesian mesh of the nacelle configuration on the coarsest refinement level is shown in Fig. 2a. Regions of additional mesh refinement are highlighted by a color distribution in Fig. 2b. The local cell length is given by

$$L_{lvl} = L_0 \cdot \left(\frac{1}{2}\right)^{lvl} \tag{7}$$

where lvl is the cell refinement level and L_0 is the mesh base length, which in this case corresponds to the longest mesh

(a) Computational mesh of the nacelle configuration on the coarsest level.

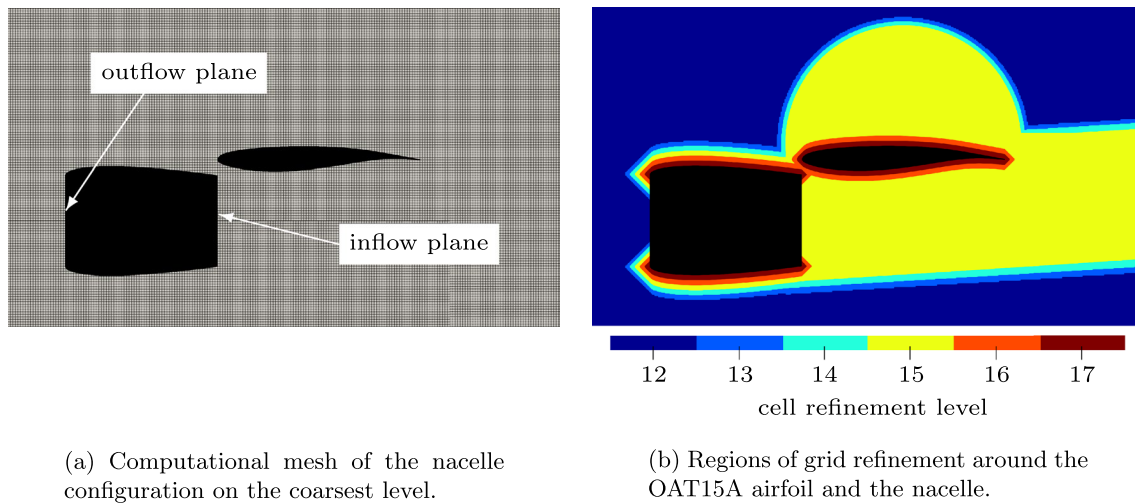(b) Regions of grid refinement around the OAT15A airfoil and the nacelle.

Fig. 2 Overview of the computational mesh of the nacelle configuration, by courtesy of Lürkens et al. [18]
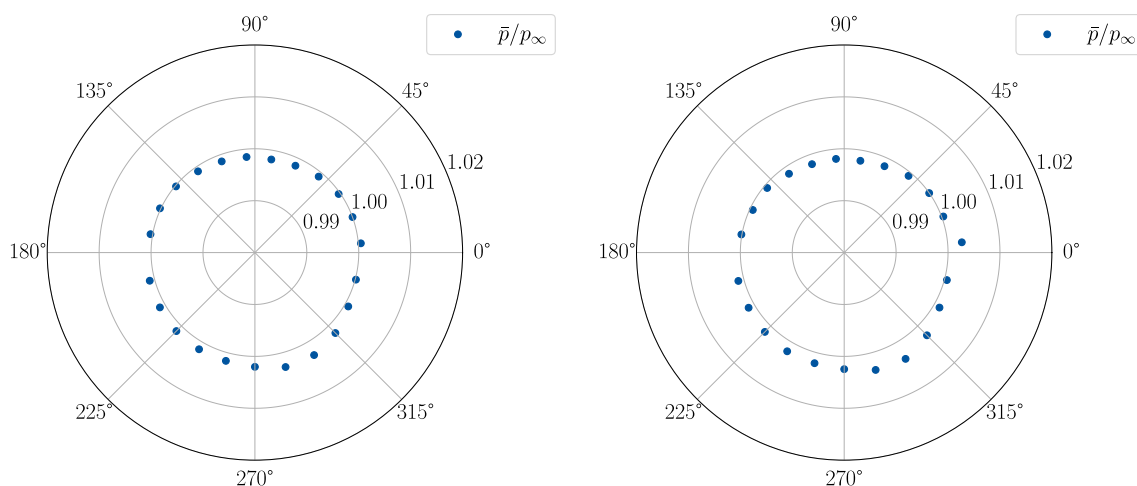

Fig. 3 Farfield mean pressure conditions for the baseline configuration (left) and the nacelle configuration (right)

dimension of $L_x = 25.4c$. The resulting number of Cartesian cells for both configurations is given in Table 1.

The wall-model is applied to all solid wall boundaries. Following the requirements proposed by Kawai and Larsson [30] the evaluation distance h_{wm} of the wall-model is set to a distance of approximately three cell lengths from the wall. A characteristic outflow boundary condition is used for the main outflow plane to suppress spurious reflections. Standard in- and outflow boundary conditions with sponge layers are applied to the remaining in- and outflow planes in the x- and y-direction. Periodicity is applied to spanwise boundaries, which is a great simplification of the in general highly three-dimensional flow field around the engine nacelle. This, however, allows the study of the effect of the upstream shock wave and the free-shear layer introduced by the nacelle geometry onto the buffet phenomenon while keeping the total number of grid points at a manageable level. At the nacelle inlet, a standard outflow boundary condition is applied. For the engine outlet, a 1/7th power law velocity profile is prescribed while maintaining mass conservation with the engine inlet. Hence, the setup represents a simple flow-through nacelle.

To enforce a controlled transition of the boundary layer into a turbulent state, the tripping method by Schlatter and Örlü [31] is employed at $x/c = 0.07$ on both sides of the airfoil.

4 Results

For both setups, data were collected for about 70 convective time units $CTU = c/u_\infty$ which means the lower resolution limit is $Sr_{min} \approx 0.014$. Spanwise averaged surface data of the OAT15A airfoil and the nacelle were sampled at a sampling interval of $4.1 \cdot 10^{-3} \, CTU$ at every 1% of the airfoil's

Table 1 Mesh size of the baseline configuration without nacelle and the configuration including the nacelle

	Baseline	With nacelle
Number of cells	$0.73 \cdot 10^9$	$1.24 \cdot 10^9$

chord length. In addition, wall normal velocity and pressure profiles were determined at every 5% of the airfoil's chord length at the same sampling interval of $4.1 \cdot 10^{-3} \, CTU$. According to the Nyquist–Shannon theorem, the highest resolvable frequency is at half the sampling frequency, such that $Sr_{max} \approx 122$. For the analysis of the shock dynamics with DMD, volumetric data of the flow field were collected at a sampling interval of 0.1025 CTU such that the DMD is able to capture dynamic phenomena up to $Sr_{max}^{DMD} = 4.87$.
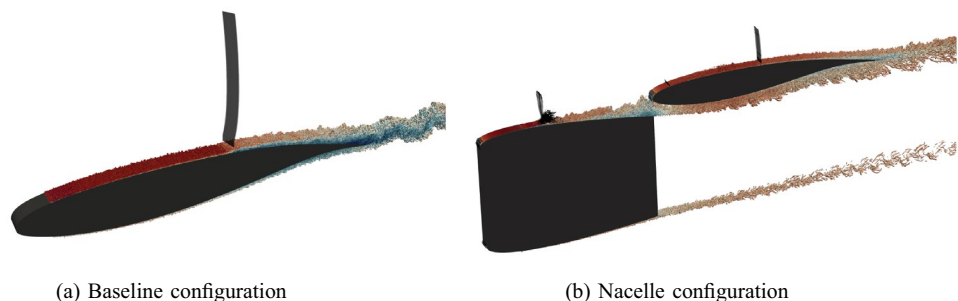
4.1 General flow field

In Fig. 4, instantaneous contours of the Q-criterion [32] and the pressure gradient are given for both configurations illustrating the turbulent boundary layer on the airfoil and the nacelle as well as the shock waves on the airfoil and the nacelle. It is obvious that the wake on the upper part of the nacelle merges with the boundary layer on the airfoil suction side. In Fig. 5a, the airfoil's mean and instantaneous pressure coefficients at the most upstream and most downstream shock position are shown for both configurations. This is complemented by the mean pressure coefficient on the nacelle upper part given in Fig. 5c. It is remarkable that the modeling of the engine nacelle as a flow-through nacelle affects the pressure side only marginally. It is, however, obvious that the integration of the nacelle leads to a significantly weaker shock and an upstream displacement of the mean shock location on the suction side. The mean shock position is determined at approximately $x_s = 0.53$ for the baseline configuration and $x_s = 0.47$ for the configuration including the nacelle. Considering the most upstream and most downstream shock locations, the nacelle configuration exhibits a noticeably lower amplitude in the shock dynamics compared to the baseline configuration. This finding is supported by the time-resolved pressure signal at the mean shock position shown in Fig. 6a. After a transient phase the baseline configuration is characterized by a stable—almost harmonic—oscillation. The pressure signal of the nacelle configuration, however, exhibits highly variable dynamics of noticeably lower amplitude. The frequency spectra of these pressure signals are shown in Fig. 7a and b. The

Fig. 4 Instantaneous contours of the Q-criterion colored by the local Mach number. Shocks are visualized by contours of the pressure gradient
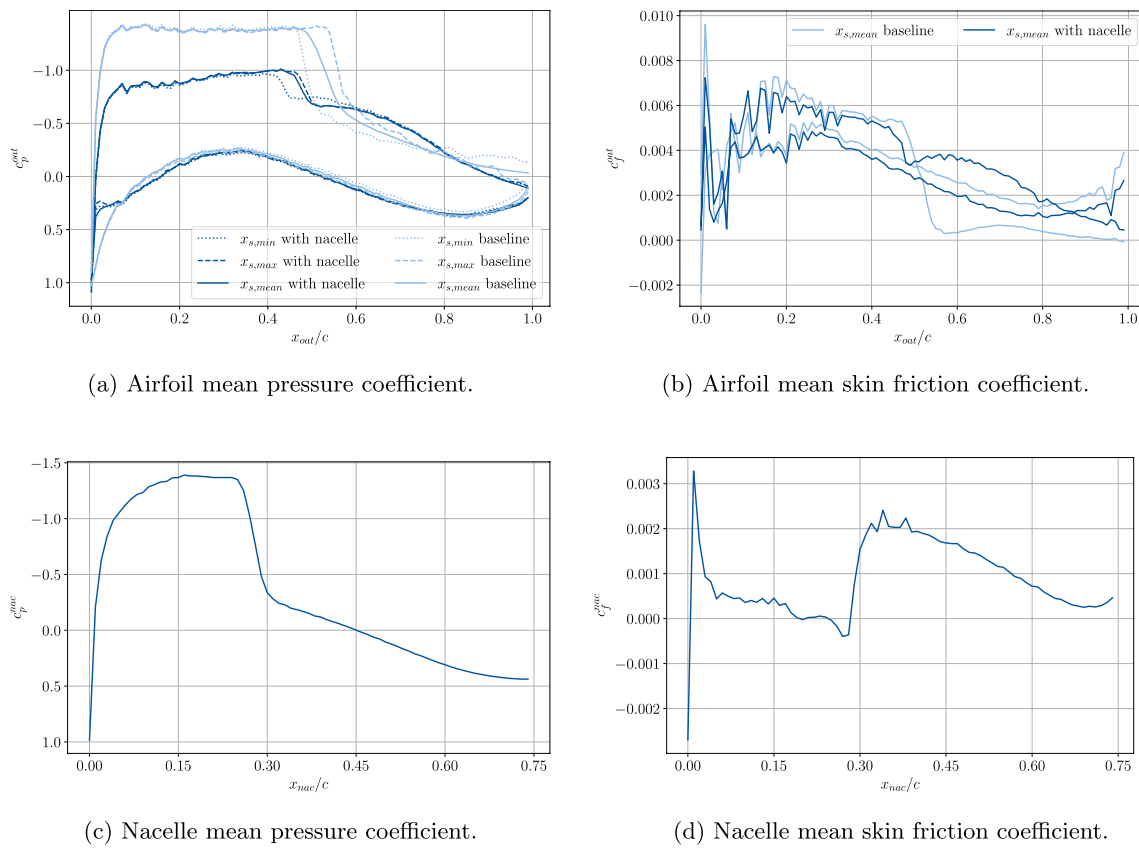
(a) Baseline configuration

(b) Nacelle configuration

(a) Airfoil mean pressure coefficient.

(b) Airfoil mean skin friction coefficient.

(c) Nacelle mean pressure coefficient.

(d) Nacelle mean skin friction coefficient.

Fig. 5 Mean pressure and skin-friction coefficients on airfoil and nacelle upper part

(a) Time history of the surface pressure at the mean shock position for both configurations.

(b) Correlation coefficient of the low-pass filtered pressure signal at the mean shock position on nacelle and airfoil.
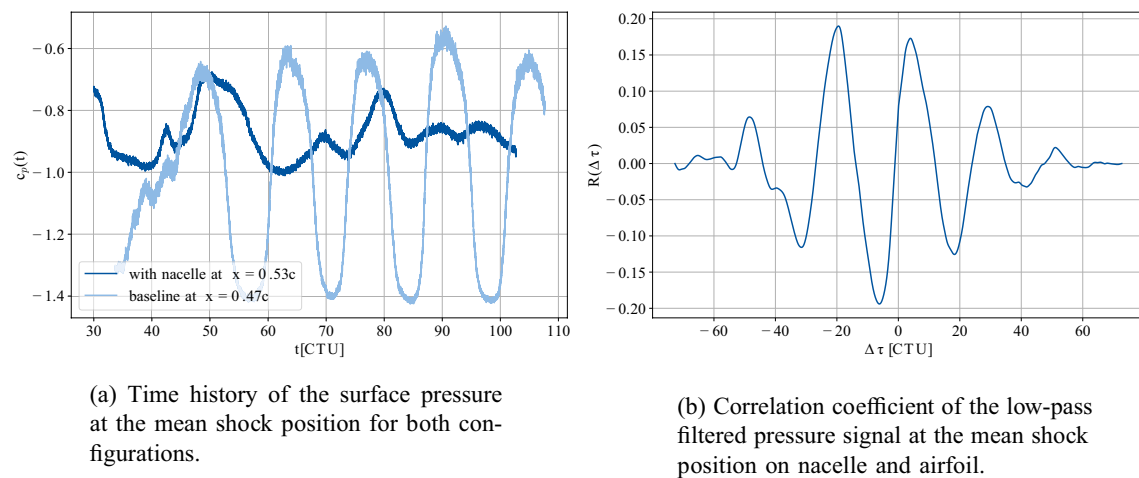
Fig. 6 Time series data at the mean shock position

consistent low-frequency shock oscillation of the baseline configuration is evidenced in a clear peak at $Sr = 0.072$. The spectrum of the nacelle configuration, however, is characterized by a much more broadband peak in the range of $0.03 < Sr < 0.04$ with the expected lower amplitude.

An additional peak at $Sr = 2.0$ is prominent, which is not observed in the baseline configuration. For the nacelle configuration, the correlation coefficient between the pressure signal at the nacelle shock position and the airfoil shock position was computed according to

(a) baseline: $x_{s,mean} = 0.53c$

(b) with nacelle $x_{s,mean} = 0.47c$
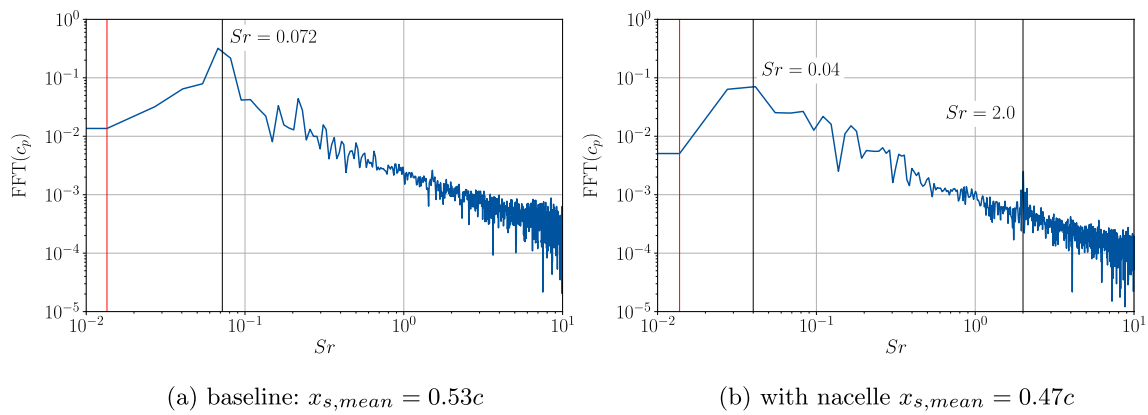
Fig. 7 FFT of the pressure signal at the mean shock position for both configurations. The red line indicates the lower resolution limit $Sr_{min} \approx 0.014$

$$R(\Delta\tau) = \sum_{-\infty}^{\infty} \frac{c_{p'}^{nac}(t)c_{p'}^{oat}(t + \Delta\tau)}{\sigma(c_{p'}^{nac}(t))\sigma(c_{p'}^{oat}(t))}. \tag{8}$$

Its distribution is given in Fig. 6b. The quantity $c_{p'}$ corresponds to the part of c_p fluctuating around its mean and σ denotes the standard deviation. We find maximum positive correlation at a time lag of $\Delta\tau = -20\,CTU$ which suggests the nacelle shock is affected by the dynamics of the airfoil shock.

The c_f plot on the nacelle in Fig. 5d shows a flow separation in the shock impingement region. Note the oscillating c_f distribution upstream of the separation region and downstream of the shock. We associate this with the wall-model which implies an attached and quasi-steady turbulent boundary layer flow in a region of flow transition. This is supported by the skin-friction coefficient on the airfoil (Fig. 5b) downstream of the tripping region showing similar behavior for $x/c < 0.35$. Since these fluctuations in the c_p and c_f distributions smooth

out upstream of the shock region, we assume no massive effects on the shock dynamics.

To understand this alteration to the shock dynamics, the disturbance of the flow onto the airfoil due to the integration of the engine nacelle will be considered next. In Fig. 8a, the deviation of the local flow angle of the nacelle configuration from the baseline configuration given by

$$\Delta\alpha = \arctan\left(\frac{\bar{u}}{\bar{v}}\right)_{nac} - \arctan\left(\frac{\bar{u}}{\bar{v}}\right)_{base} \tag{9}$$

is shown. It is evident that immediately upstream of the airfoil the flow is deflected to smaller angles of attack by the contour of the engine nacelle. In Fig. 8b, the deviation of the local Mach number of the nacelle configuration from the baseline configuration defined by

$$\Delta Ma = \left(\frac{|\bar{u}|}{\sqrt{\gamma\bar{p}/\bar{\rho}}}\right)_{nac} - \left(\frac{|\bar{u}|}{\sqrt{\gamma\bar{p}/\bar{\rho}}}\right)_{base} \tag{10}$$

(a) Flow angle deviation $\Delta\alpha$. Black lines show iso-contours at $\Delta\alpha = -3.5°$.

(b) Mach number deviation ΔMa. Black lines show iso-contours at $\Delta Ma = -0.1$.
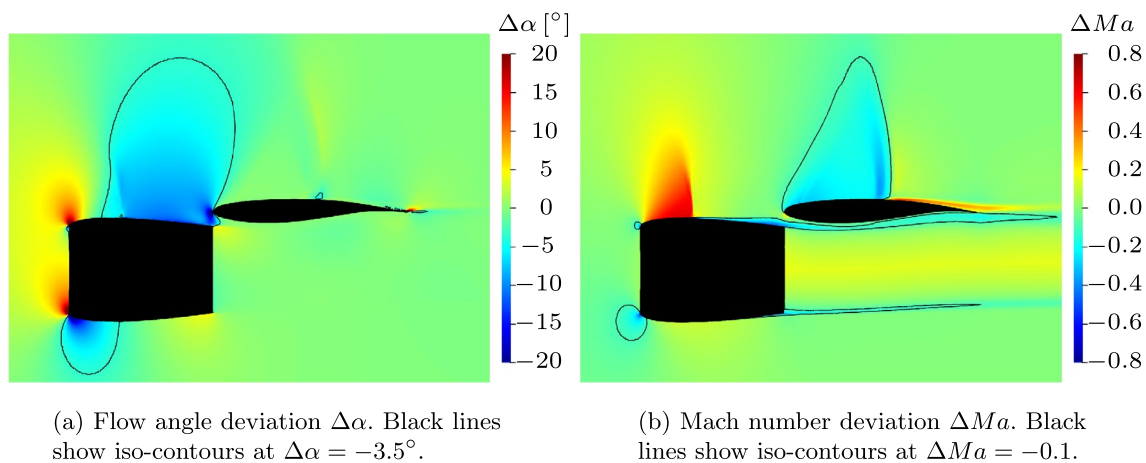
Fig. 8 Deviation of the flow field of the nacelle configuration from the baseline configuration

is shown. As a consequence of the shock and the boundary layer on the upper part of the nacelle, the Mach number of the flow onto the airfoil is significantly reduced.

The buffet phenomenon is, however, highly sensitive to the angle of attack and the Mach number. Considering the numerical and experimental studies on the OAT15A airfoil at comparable conditions [2, 13, 27], it is reasonable that the reduction of the angle of attack and the Mach number due to the integration of the engine nacelle results in a shift of the dynamics from fully developed buffet to pre-developed buffet. Furthermore, the Mach number in the free-shear layer downstream of the trailing edge is evidently affected by the integration of the nacelle (Fig. 8b). As already seen in Fig.4b, the wake flow from the upper part of the nacelle interacts with the boundary layer on the pressure side of the airfoil leading to a reduced local Mach number. On the suction side, the weaker shock wave leads to a reduced flow deceleration and to a weaker boundary layer separation and thus, to a higher local Mach number.

Contours of p'_{rms} of both configurations are depicted in Fig. 9a and b. The more upstream mean shock position and the lower amplitude of the shock oscillation indicated by Fig. 5a are confirmed. In addition, the pressure fluctuations of the nacelle configuration are massively reduced. Therefore, the integration of the engine nacelle cannot merely be considered as a perturbation of the global flow topology, but also has a notable impact on the acoustics between trailing edge and shock wave. The shock-induced separation on the suction side and the noise generated by the trailing edge shear flow, however, are essential to established buffet models [1, 6]. This means the alteration of the shock dynamics due to the integration of the nacelle does have an important impact on the overall aerodynamics of the system.

4.2 DMD analysis

To further analyze the dynamics and investigate the underlying physical mechanisms with respect to established buffet models, SP-DMD was performed on data of the pressure and the streamwise velocity field. The penalty parameter β of the SP-DMD algorithm was varied to obtain only the most relevant modes. The performance loss defined by

$$\Pi_{loss} = \frac{\|V_1^N - \phi D_a V_{and}\|_F}{\|V_1^N\|_F} \cdot 100\% \qquad (11)$$

gives the relative deviation of the reconstructed field from the original snapshot sequence and allows the evaluation of the quality of the flow field reconstruction from the selected modes. More details on the SP-DMD algorithm are given in Jovanović et al. and Feldhusen-Hoffmann et al. [8, 26].

Performing SP-DMD on the pressure field data of the baseline configuration with $\beta = 31257.44$ leaves only one relevant mode at a frequency of $Sr = 0.072$ which agrees well with the peak found in the FFT results of the surface pressure signal at the mean shock position given in Fig. 7a. The resulting DMD spectrum is given in Fig. 13a. Since the mode selected by the SP-DMD is on the unity circle, we can expect this mode to be stable. Contours of the mode's amplitude are given in Fig. 10a. They clearly show the association with the shock buffet. The performance loss at the given β is 1.7% such that in return 98.3% of the dynamics of the pressure field can be reconstructed using only this mode and its complex conjugate. Lowering the penalty parameter β merely introduces upper or lower harmonics of the buffet frequency into the DMD spectrum. From that, it is obvious that the dynamics of the pressure field is solely dominated by the buffet mode. The corresponding mode of the streamwise velocity field at the same frequency of $Sr = 0.072$ is given in Fig. 10b. Apart from the shock movement, this mode also reveals the periodic thickening and shrinking of the boundary layer past the shock wave, which is essential for established buffet models [1, 6]. It is remarkable that there are two regions of changing sign in the vicinity of the trailing edge. These regions coincide with the peaks in the pressure fluctuations shown in Fig. 9a. The change of sign in the streamwise velocity mode implies a temporal variation of the local shear rate. Fluctuations in the local shear rate are,
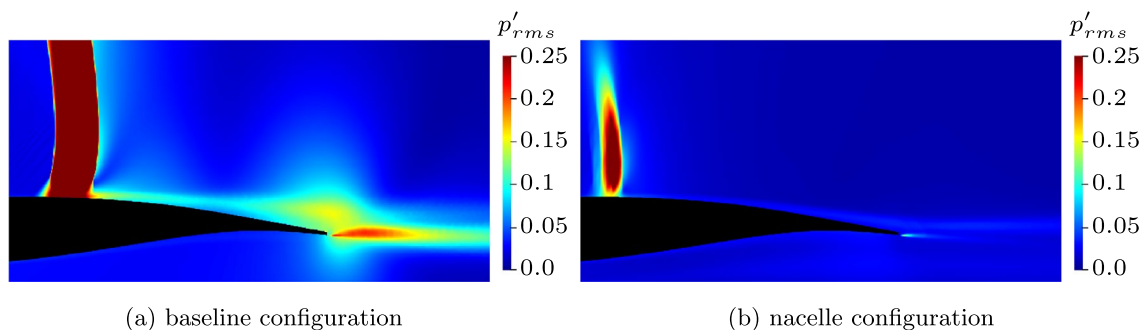

(a) baseline configuration

(b) nacelle configuration

Fig. 9 Contours of p'_{rms} of the baseline configuration and the nacelle configuration
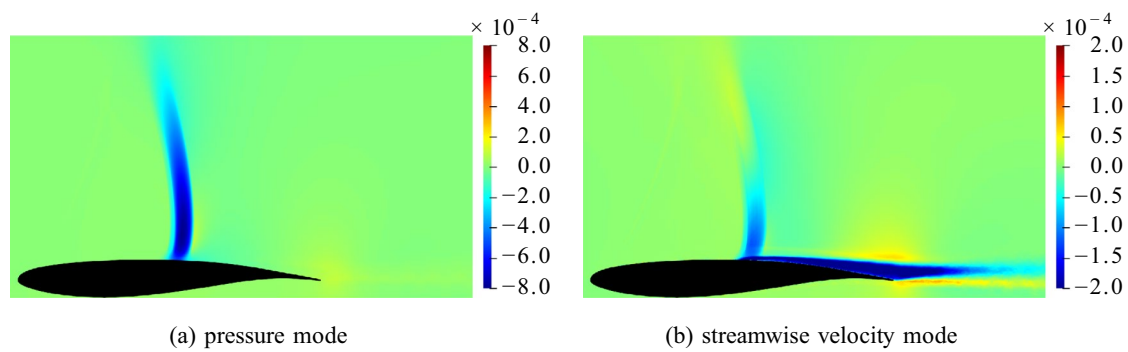
(a) pressure mode

(b) streamwise velocity mode

Fig. 10 Buffet modes at $Sr = 0.072$ of the pressure and the streamwise velocity fields of the baseline configuration

however, part of the driving acoustic source term in free-shear flows, which is the perturbed Lamb vector given by

$$L' = (\boldsymbol{\omega} \times \boldsymbol{u})' \tag{12}$$

where $\boldsymbol{\omega}$ is the vorticity vector [33]. One can conclude that the origin of the pressure fluctuations in the vicinity of the trailing edge is due to acoustic perturbations which agrees well with the established buffet models [1, 6]. It should also be noted that both the pressure and velocity modes have a Ritz eigenvalue of close to 1 such that the transient component of these modes is negligible.

Performing SP-DMD on the pressure field data of the nacelle configuration with $\beta = 24770.98$ leaves a single remaining mode at a frequency of $Sr = 2.01$. A peak at this very frequency was already found in the FFT results in Fig. 7b. The real parts of the corresponding pressure and streamwise velocity modes are shown in Fig. 11a and b. It is obvious that this dynamic feature is restricted almost completely to the flow on the upper surface of the nacelle and can be associated with the shock-induced variation of the boundary layer on the nacelle and the subsequent vortex generation. The order of magnitude of the frequency generally agrees well with the findings of Moise et al. [34] who

investigated the effect of boundary layer tripping on the buffet characteristics. The vortices passing over the trailing edge of the nacelle primarily convect along the pressure side of the airfoil and are subject to substantial dissipation. On the suction side, these structures are only poorly established. In particular, the shock wave on the airfoil suction side exhibits no considerable dynamic features and appears to be negligibly affected at this frequency.

Lowering the penalty parameter to $\beta = 12328.57$ includes the low-frequency mode at $Sr = 0.043$ which agrees well with the plateau-like low-frequency region in Fig. 7b. The resulting DMD spectrum is given in Fig. 13b. Again, all modes selected by the SP-DMD are on the unity circle and therefore stable. The real part of the corresponding pressure mode is given in Fig. 12a. The corresponding streamwise velocity mode is detected at a slightly higher frequency of $Sr = 0.047$ and is shown in Fig. 12b. It is remarkable that both the nacelle and the airfoil shock display dynamic features at the respective frequency which agrees well with the correlation coefficient given in Fig. 6b. The spatial amplitude of the shock motion, however, is clearly smaller compared to the buffet found for the baseline configuration. Considering the flow field disturbances by the nacelle geometry discussed in Sect. 4.1, this supports the suggestion that
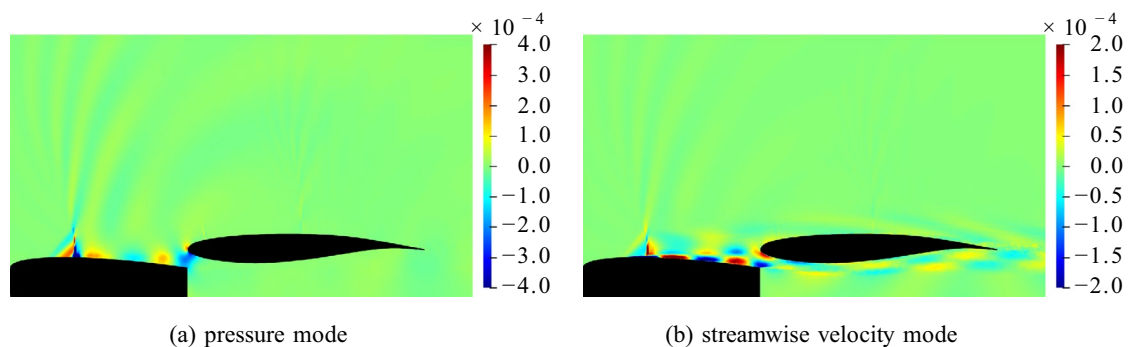

(a) pressure mode

(b) streamwise velocity mode

Fig. 11 Modes of the shock wave/boundary layer interaction at $Sr = 2.01$ of the pressure and the streamwise velocity fields of the nacelle configuration
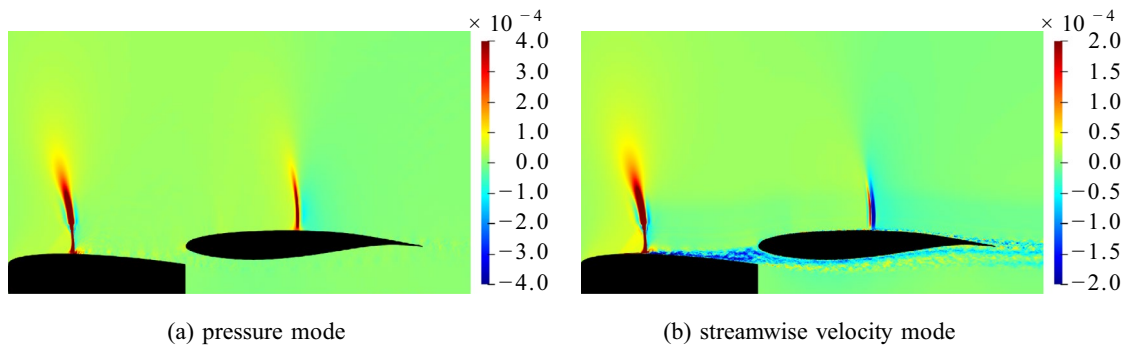
(a) pressure mode

(b) streamwise velocity mode

Fig. 12 Buffet modes of the pressure field at $Sr = 0.043$ and the streamwise velocity field at $Sr = 0.047$ of the nacelle configuration
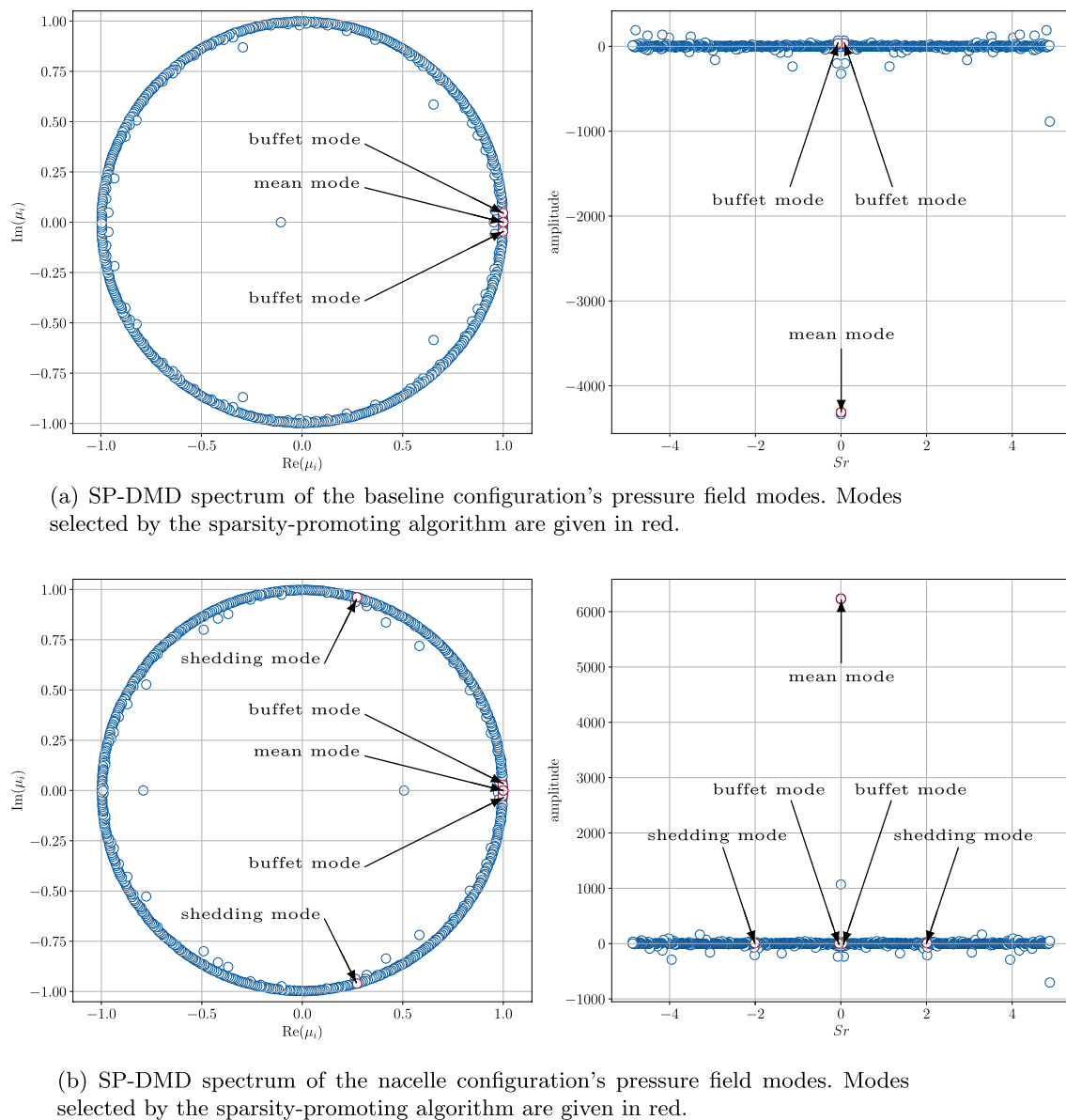

(a) SP-DMD spectrum of the baseline configuration's pressure field modes. Modes selected by the sparsity-promoting algorithm are given in red.

(b) SP-DMD spectrum of the nacelle configuration's pressure field modes. Modes selected by the sparsity-promoting algorithm are given in red.

Fig. 13 Spectral representation of the SP-DMD modes

the nacelle suppresses developed buffet at the given flow parameters and a pre-developed state of buffet is observed. The shared dynamic features, however, suggest that a coupling mechanism between the dynamics of the nacelle shock and the airfoil shock exists. Note that similar to the baseline configuration, the streamwise velocity mode exhibits a periodic behavior of the nacelle boundary layer downstream of the shock. The wake flow of the nacelle merges into the boundary layer on the airfoil pressure side, such that eventually also the trailing edge flow of the airfoil is affected by the shock dynamics on the nacelle. Thereby, a connection between the dynamics of the nacelle shock and the mechanisms of existing buffet models [1, 6] can be expected. Yet, as discussed in Sect. 4.1 the acoustic field at the airfoil trailing edge is considerably weaker for the nacelle configuration such that determining the exact mechanism will require further scrutiny including detailed investigation of the acoustic source terms in the vicinity of the trailing edge.

5 Conclusion

WM-LES of the OAT15A complemented by a generic 2D nacelle geometry and a corresponding baseline configuration without the nacelle have been performed. The baseline case exhibits a well-developed low-frequency shock oscillation at $Sr = 0.072$. Investigation of the pressure fluctuations in the vicinity of the trailing edge and the flow field dynamics extracted by means of SP-DMD agree well with established buffet models. The nacelle configuration is characterized by a system of two shocks, one on the upper part of the engine nacelle and one on the airfoil suction side. Both shocks are subject to a low-frequency oscillation at the same frequency of $Sr = 0.043$ which, however, has a smaller spatial amplitude than the buffet found for baseline configuration. The occurrence of a shared dynamic mode of the nacelle and the airfoil shock suggests the existence of a coupling mechanism, the exact determination of which requires further investigation. The analysis of the pressure field reveals a considerable attenuation of the pressure fluctuation in the vicinity of the trailing edge. Comparison of the mean flow fields of both configurations shows a significant disturbance of the flow conditions onto the airfoil. That is, both Mach number and local angle of attack are reduced by the introduction of the nacelle. The buffet phenomenon is, however, highly sensitive to variations of angle of attack and Mach number. Considering the mitigated and irregular shock dynamics, it is, therefore, stated that the altered flow conditions lead to a shift from fully developed buffet to pre-developed buffet.

The reduction of the UHBR nacelle to a 2D-periodic geometry allowed a first study of the dynamic impact a geometric perturbation upstream of the airfoil has on the overall flow topology of the airfoil and the occurring shock oscillations which define the buffet phenomenon. The existence of a mutual mode between nacelle shock and airfoil shock has consequences for future 3D investigations of nacelle airfoil interaction in transonic flow.

Declarations

References

1. Lee, B.H.K.: Self-sustained shock oscillations on airfoils at transonic speeds. Prog. Aerosp. Sci. **37**(2), 147–196 (2001). https://doi.org/10.1016/S0376-0421(01)00003-3
2. Deck, S.: Numerical simulation of transonic buffet over a supercritical airfoil. AIAA J. **43**(7), 1556–1566 (2005). https://doi.org/10.2514/1.9885
3. Xiao, Q., Tsai, H.M., Liu, F.: Numerical study of transonic buffet on a supercritical airfoil. AIAA J. **44**(3), 620–628 (2006). https://doi.org/10.2514/1.16658
4. Hartmann, A., Klaas, M., Schröder, W.: Time-resolved stereo piv measurements of shock-boundary layer interaction on a supercritical airfoil. Exp. Fluids **52**(3), 591–604 (2012). https://doi.org/10.1007/s00348-011-1074-6
5. Hartmann, A., Klaas, M., Schröder, W.: Coupled airfoil heave/pitch oscillations at buffet flow. AIAA J. **51**, 1542–1552 (2013). https://doi.org/10.2514/1.J051512
6. Hartmann, A., Feldhusen, A., Schröder, W.: On the interaction of shock waves and sound waves in transonic buffet flow. Phys. Fluids **25**(2), 026–101 (2013). https://doi.org/10.1063/1.4791603
7. Feldhusen-Hoffmann, A., Statnikov, V., Klaas, M., Schröder, W.: Investigation of shock-acoustic-wave interaction in transonic flow. Exp. Fluids **59**, 15 (2017). https://doi.org/10.1007/s00348-017-2466-z

8. Feldhusen-Hoffmann, A., Lagemann, C., Loosen, S., Meysonnat, P., Klaas, M., Schröder, W.: Analysis of transonic buffet using dynamic mode decomposition. Exp. Fluids **62**, 66 (2021). https://doi.org/10.1007/s00348-020-03111-5

9. Dietz, G., Mai, H., Schröder, A., Klein, C., Moreaux, N., Leconte, P.: Unsteady wing-pylon-nacelle interference in transonic flow. J. Aircr. **45**, 934–944 (2008). https://doi.org/10.2514/6.2007-2018

10. Spinner, S., Ralf, R.: Design of a uhbr through flow nacelle for high speed stall wind tunnel investigations. Deutscher Luft- und Raumfahrtkongress (2021). https://doi.org/10.25967/550043

11. Spinner, S., Rudnik, R.: Experimental assessment of wing lower surface buffet effects induced by the installation of a uhbr nacelle. CEAS Aeronaut. J. (2022). https://doi.org/10.1007/s13272-022-00632-z

12. Giannelis, N.F., Vio, G.A., Levinski, O.: A review of recent developments in the understanding of transonic shock buffet. Prog. Aerosp. Sci. **92**, 39–84 (2017). https://doi.org/10.1016/j.paerosci.2017.05.004

13. Jacquin, L., Molton, P., Deck, S., Maury, B., Soulevant, D.: Experimental study of shock oscillation over a transonic supercritical profile. AIAA J. **47**(9), 1985–1994 (2009). https://doi.org/10.2514/1.30190

14. Lintermann, A., Meinke, M., Schröder, W.: Zonal flow solver (ZFS): a highly efficient multi-physics simulation framework. Int. J. Comput. Fluid Dyn. **34**(7–8), 458–485 (2020). https://doi.org/10.1080/10618562.2020.1742328

15. Boris, J.P., Grinstein, F.F., Oran, E.S., Kolbe, R.L.: New insights into large eddy simulation. Fluid Dyn. Res. **10**(4–6), 199–228 (1992). https://doi.org/10.1016/0169-5983(92)90023-p

16. Meinke, M., Schröder, W., Krause, E., Rister, T.: A comparison of second- and sixth-order methods for large-eddy simulations. Comput. Fluids **31**(4), 695–718 (2002). https://doi.org/10.1016/S0045-7930(01)00073-1

17. Schneiders, L., Günther, C., Meinke, M., Schröder, W.: An efficient conservative cut-cell method for rigid bodies interacting with viscous compressible flows. J. Comput. Phys. **311**, 62–86 (2016). https://doi.org/10.1016/j.jcp.2016.01.026

18. Lürkens, T., Meinke, M., Schröder, W.: Wall-modeled LES of buffet under the influence of engine nacelle flow. Deutscher Luft- und Raumfahrtkongress (2022). https://doi.org/10.25967/570433

19. Fukushima, Y., Kawai, S.: Wall-modeled large-eddy simulation of transonic airfoil buffet at high reynolds number. AIAA J. **56**(6), 2372–2388 (2018). https://doi.org/10.2514/1.J056537

20. Spalding, D.B.: A Single Formula for the "Law of the Wall". J. Appl. Mech. **28**(3), 455–458 (1961). https://doi.org/10.1115/1.3641728

21. Schmid, P.J.: Dynamic mode decomposition of numerical and experimental data. J. Fluid Mech. **656**, 5–28 (2010). https://doi.org/10.1017/S0022112010001217

22. Kou, J., Zhang, W.: An improved criterion to select dominant modes from dynamic mode decomposition. Eur. J. Mech. B/Fluids **62**, 109–129 (2017). https://doi.org/10.1016/j.euromechflu.2016.11.015. https://www.sciencedirect.com/science/article/pii/S0997754616302990

23. Kou, J., Le Clainche, S., Zhang, W.: A reduced-order model for compressible flows with buffeting condition using higher order dynamic mode decomposition with a mode selection criterion. Phys. Fluids **30**(1), 016–103 (2018). https://doi.org/10.1063/1.4999699

24. Gao, C., Zhang, W., Kou, J., Liu, Y., Ye, Z.: Active control of transonic buffet flow. J. Fluid Mech. **824**, 312–351 (2017). https://doi.org/10.1017/jfm.2017.344

25. Poplingher, L., Raveh, D.E., Dowell, E.H.: Modal analysis of transonic shock buffet on 2d airfoil. AIAA J. **57**(7), 2851–2866 (2019). https://doi.org/10.2514/1.J057893

26. Jovanović, M.R., Schmid, P.J., Nichols, J.W.: Sparsity-promoting dynamic mode decomposition. Phys. Fluids **26**(2), 024–103 (2014). https://doi.org/10.1063/1.4863670

27. Schauerte, C.J., Schreyer, A.M.: Experimental analysis of transonic buffet conditions on a two-dimensional supercritical airfoil (under review). AIAA J. (2022)

28. Zauner, M., Sandham, N.D.: Wide domain simulations of flow over an unswept laminar wing section undergoing transonic buffet. Phys. Rev. Fluids **5**, 083–903 (2020). https://doi.org/10.1103/PhysRevFluids.5.083903

29. Moise, P., Zauner, M., Sandham, N.D.: Large eddy simulations and modal reconstruction of laminar transonic buffet (under revision). J. Fluid Mech. (2021)

30. Kawai, S., Larsson, J.: Wall-modeling in large eddy simulation: length scales, grid resolution, and accuracy. Phys. Fluids **24**(1), 015–105 (2012). https://doi.org/10.1063/1.3678331

31. Schlatter, P., Örlü, R.: Turbulent boundary layers at moderate reynolds numbers: inflow length and tripping effects. J. Fluid Mech. **710**, 5–34 (2012). https://doi.org/10.1017/jfm.2012.324

32. Hunt, J.C.R., Wray, A., Moin, P.: in Center for Turbulence Research Report, CTR-S88, pp. 193–208 (1988)

33. Ewert, R., Schröder, W.: Acoustic perturbation equations based on flow decomposition via source filtering. J. Comput. Phys. **188**(2), 365-398. https://doi.org/10.1016/S0021-9991(03)00168-2

34. Moise, P., Zauner, M., Sandham, N., Timme, S., He, W.: Transonic buffet characteristics under conditions of free and forced transition. AIAA J. pp. 1–16 (2022). https://doi.org/10.2514/1.J062362